ChemSusChem

Research Article
doi.org/10.1002/cssc.202301080

Chemistry Europe
European Chemical Societies Publishing

www.chemsuschem.org

# Quantifying the Resistive Losses of the Catalytic Layers in Anion-Exchange Membrane Fuel Cells

John C. Douglin[+],[a] Kalimuthu Vijaya Sankar[+],[a, b] Ana Laura G. Biancolli,[c] Elisabete I. Santiago,[c] Yoed Tsur,*[a, b] and Dario R. Dekel*[a, b]

The existing gap in the ability to quantify the impacts of resistive losses on the performance of anion-exchange membrane fuel cells (AEMFCs) during the lifetime of their operation is a serious concern for the technology. In this paper, we analyzed the ohmic region of an operating AEMFC fed with pure oxygen followed by $CO_2$-free air at various operating currents, using a combination of electrochemical impedance spectroscopy (EIS) and a novel technique called impedance spectroscopy genetic programming (ISGP). Presented here for the first time in this work, we isolated and quantified the individual effective resistance ($R_{eff}$) values occurring in the AEMFC and their influence on performance as operating conditions change. We believe that this first work is vital to help distinguish the influence of the individual catalytic and mass-transfer processes in this technology thereby providing valuable data to the AEMFC community, with potentially wider applicability to other electrochemical devices where individual physical processes occur simultaneously and need to be sequestered for deeper understanding.

## Introduction

Hydrogen powered fuel cells have been offered as an attractive alternative to fossil fuels on account of the cleanliness of hydrogen and the high efficiency of fuel cell devices.[1–3] Among the various types of fuel cells, anion exchange membrane fuel cells (AEMFCs), consisting of a solid membrane in an alkaline operating environment, have gained noteworthy interest within the energy research community, mainly due to the potential of using critical raw material (CRM)-free catalysts and low-cost polymeric membranes.[4–9]

[a] J. C. Douglin,[+] Dr. K. Vijaya Sankar,[+] Prof. Y. Tsur, Prof. D. R. Dekel
The Wolfson Department of Chemical Engineering
Technion, Israel Institute of Technology
Haifa, 3200003 (Israel)
E-mail: dario@technion.ac.il
tsur@technion.ac.il
Homepage: https://dekel.technion.ac.il/
https://electroceramics.net.technion.ac.il/

[b] Dr. K. Vijaya Sankar,[+] Prof. Y. Tsur, Prof. D. R. Dekel
The Nancy & Stephen Grand Technion Energy Program (GTEP)
Technion – Israel Institute of Technology
Haifa 3200003 (Israel)
E-mail: dario@technion.ac.il
tsur@technion.ac.il
Homepage: https://dekel.technion.ac.il/
https://electroceramics.net.technion.ac.il/

[c] Dr. A. L. G. Biancolli, Prof. E. I. Santiago
Nuclear and Energy Research Institute, IPEN/CNEN, 05508-000
São Paulo (Brazil)

[+] These authors contributed equally to this work.

Supporting information for this article is available on the WWW under https://doi.org/10.1002/cssc.202301080



At the fundamental level, the current versus voltage (I–V or polarization curve) relationship is the most vital performance indicator of an AEMFC and can be used to singularly encapsulate the major overpotential losses from the thermodynamic cell potential (1.229 V). These overpotential losses can be further characterized as (i) charge transfer resistive losses in the anode catalyst layer and cathode catalyst layer as the catalyst is required to overcome the activation energy barriers for their respective reactions. These are commonly referred to as kinetic losses. (ii) Losses due to both ionic and electronic conducting components, such as bipolar plates, gas diffusion layers, catalyst layers, and the membrane as current is drawn are referred to as the ohmic losses. (iii) Losses due to the limited rate of reactant and product diffusion through the porous media at higher currents are referred to as mass transfer losses.[10–17]

Despite this general knowledge of the major overpotentials in AEMFCs, there is still a gap in the ability to quantify the effective resistances ($R_{eff}$) from the individual cell processes (Scheme 1). Unravelling this mystery would facilitate paths to deeper insights about catalyst efficiency, ionomer and membrane degradation and the effect of the oxidant (air with or without $CO_2$) during the lifetime of the operating fuel cell.

In this work, we analyze and report for the first time the results of a study of the ohmic region of an operando AEMFC. Using a combination of electrochemical impedance spectroscopy (EIS) and impedance spectroscopy genetic programming (ISGP) techniques, we quantify the individual resistive losses of the simultaneous AEMFC processes while operating with both pure oxygen and $CO_2$-free air as the cathode oxidant.

EIS is a non-destructive electrochemical technique, which is typically used to understand the resistance/capacitance contributed by various processes. In the AEMFC literature, EIS has been used extensively as both an ex-situ method to gauge $OH^-$ transport resistance through AEMs,[18–21] or in-situ to quantify the various voltage losses and determine overall fuel cell performance by analyzing Nyquist plots via modelling equiv-

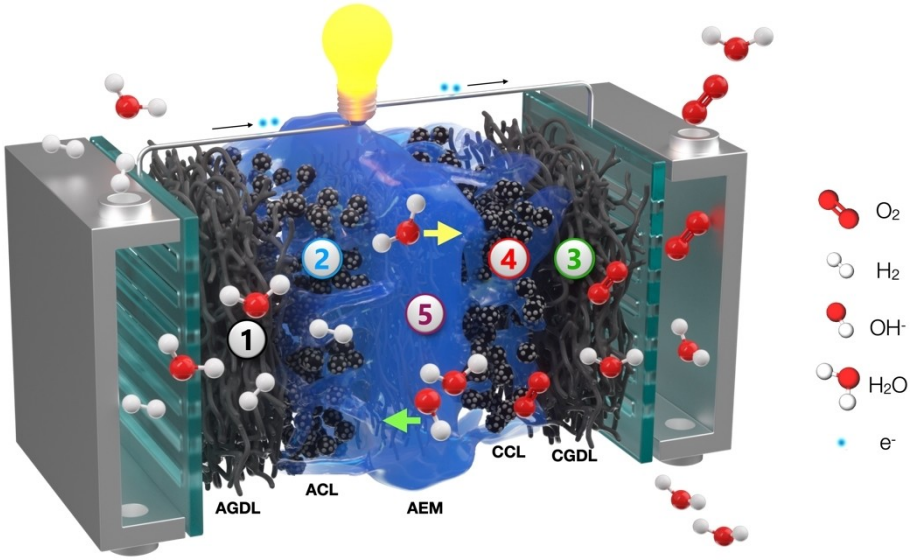


**Scheme 1.** Schematic of a $H_2$-powered AEMFC depicting the simultaneously occurring cell processes. ① Humidified $H_2$ diffuses through the anode gas diffusion layer (AGDL) to the reaction sites of the anode catalyst layer (ACL) ② where the hydrogen oxidation reaction (HOR), $H_2 + 2OH^- \rightarrow 2H_2O + 2e^-$, takes place and electrons are drawn through the circuit to power the lightbulb, ③ humified $O_2$ diffuses through the cathode gas diffusion layer (CGDL) to the reaction sites of the cathode catalyst layer (CCL) ④ where electrons from the circuit react in the oxygen oxidation reaction (ORR) $1/2O_2 + H_2O + 2e^- \rightarrow 2OH^-$, ⑤ the $OH^-$ ions from the ORR conduct through the anion-exchange membrane (AEM) from the cathode to the anode to take part in the HOR, while $H_2O$ (final product from the AEMFC) produced from the HOR simultaneously diffuses in the opposite direction across the AEM to take part in the ORR.

alent circuits (ECs).[22–29] However, fitting the EIS spectra measured at different conditions within the studied system may not lead to similar ECs, resulting in a lack of reliability of the obtained parameters.

To avoid some of these issues, it is plausible to transfer the data gathered from the frequency domain into the time domain and study the distribution function of relaxation times – DFRT, also known as DRT. This can be done via various approaches including Fourier transform,[30] Ridge regularization,[31] Tikhonov regularization,[32] and Maximum entropy.[33] The Tsur group has developed a genetic programming method to obtain an analytical DFRT rather than a point-by-point one. This unique technique focuses on isolating and quantifying physical phenomena for various electrochemical applications via artificial intelligence.[34–40] The ISGP software intrinsically avoids overfitting and the use of filters or tweaking parameters (see detailed information about ISGP in the experimental section and SI).

## Results and Discussion

### AEMFC Test Results

The AEMFC (materials, fabrication[41–50] and testing details are found in the experimental section below) was first tested at a temperature of 80 °C under hydrogen and oxygen gases at 1 slpm with equal humidification (relative humidity of 88 %) and back-pressure (BP of 100 kPa) on both electrodes, to reduce mass transfer related losses and extend the ohmic region profile (Figure 1). At stable operating conditions, the optimized results yielded a limiting current upwards of 9 A (current density of 4.25 A cm$^{-2}$) and a peak power density of ca. 1.2 W cm$^{-2}$ (black lines with small, closed circles in Figures 1a, b), respectively.

The effects of the BP on the electrodes can be seen in the same figures (Figures 1a, b). First, we removed the BP from the cathode (dashed blue lines with open circles indicating 100 kPa on anode only), which resulted in a sharp drop in performance by about half, both in the limiting current and peak power density values. This indicates either the mass transport resistance in the cathode has increased giving way to flooding or drying and/or the ionic resistivity within of the AEM was affected.

Next, we removed the BP completely from both the anode and cathode (dashed yellow lines in Figures 1a, b), and the performance dropped to slightly lower than the previous operating condition wherein 100 kPa of BP was applied to the anode only. It is also worthy to note that the orange polarization curve (without BP) has the lowest voltage values in comparison to the other curves (Table 1) within the studied ohmic region (inset of Figure 1a). These results are indicative of increases in the mass transport resistance within both electrodes and to the ionic resistivity of the AEM given the steeper gradient within the ohmic region of the orange curve. However, it cannot be possible to quantify the individual contribution of each electrode to the total resistance.

Afterwards, we applied 100 kPa of BP to the cathode (dashed green lines with small, closed circles indicating 100 kPa on cathode only). An increase in both the limiting current and peak power density values are seen (Figures 1a, b). These results indicate that applying BP on the cathode only has a more substantial effect than when no BP is applied, or in the case of when only the anode is pressurized. The inset of Figure 1a shows that the green curve has more gradual decline in the

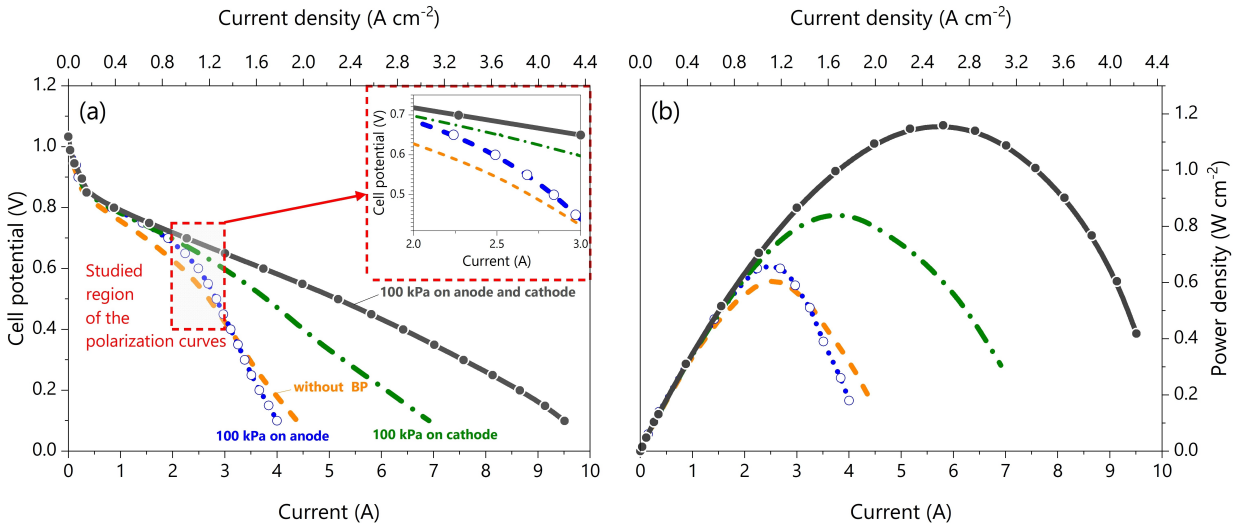


**Figure 1.** $H_2$—$O_2$ AEMFC operated with 1 slpm gas flows at 80 °C, equal humidification (relative humidity of 88 %) and BP of 100 kPa on both electrodes. The currents were varied at 2, 2.5 and 3 A to collect EIS data. BP was further adjusted at the 3 A current load and EIS data collected to investigate the effects of BP on the anode only (100 kPa), on the cathode only (100 kPa), and no BP (a) Polarization curves with zoomed-in area showing region studied using a combination of EIS and ISGP (b) corresponding I–P curves. A 2.25 $cm^2$ single five-layer membrane electrode assembly (MEA) was used.

slope within the ohmic region, i.e., higher voltage values in comparison to the yellow (without BP) and blue (100 kPa on anode only) curves (Table 1), implying lower membrane resistivity in that case.

The cathode oxidant was then switched to $CO_2$-free air and BP returned to 100 kPa on both electrodes with all the other operating conditions held at the same values. Then, the voltage was held at 0.5 V for 1 h to allow the cell to stabilize at the new operating conditions. Afterwards, seven successive polarization scans were performed within 5-minute intervals of each other. The composite results are shown with error bars in Figures S1(a, b). As expected, the fuel cell performance declined on account of the reduction of $O_2$ content to 21 %, resulting in limiting current slightly higher than 5 A (current density of 2.3 A $cm^{-2}$) and peak power density value upwards of 0.6 W $cm^{-2}$ (Figure S1). Furthermore, while the studied region (insert of Figure S1a) of the polarization curve under $CO_2$-free air mode has shifted much closer to the high-current density region, it is still within the ohmic region.

## EIS and ISGP Results

In order to bring further understanding to the resistive losses of the AEMFC operated at various conditions, and quantify the individual contributions to the total losses, we gathered EIS data at each operating condition for further analysis by ISGP (further details about EIS and ISGP can be found in the experimental section below). The Nyquist plots correlating to the EIS data of the AEMFC operated in $H_2$—$O_2$ with 1 slpm gas flows at 80 °C with equal humidification (relative humidity of 88 %) and back-pressurization (100 kPa) on both electrodes measured at 2, 2.5, and 3 A, are shown in Figure 2. The Nyquist plot shows negative imaginary impedance values against the real impedance values in a broad frequency range. Two depressed arcs are observed in both the high and low frequency regions. The high-frequency arcs are caused by charge transfer resistances and the low-frequency arcs represent mass transfer processes.[29] Depressed arcs usually translate into broader distributions of time constants or relaxation times within the measured frequency range, while the starting point of the high-frequency arc is related to ohmic resistances through the membrane.[51] An interesting observation is that the diameters of the arcs do not change drastically with an increase in drawn current.

The frequency-domain data was converted into time-domain distribution function of relaxation times (DFRT) data via ISGP.[51] The DFRT (Figures 3a,b) consists of four peaks (P2, P3, P4, P5) within the measured frequency range and one peak (P1) outside the range, at high frequencies or low relaxation times.

**Table 1.** Voltage values corresponding to measured current values of 2, 2.5 and 3 A when the AEMFC was operated using $H_2$—$O_2$ with 1 slpm gas flows at 80 °C, equal humidification (relative humidity of 88 %) and varied back-pressures (BPs) on both electrodes.

| Measured current (A) | 100 kPa BP on anode and cathode (V) | 100 kPa BP on anode only (V) | 100 kPa BP on cathode only (V) | Without BP (V) |
|---|---|---|---|---|
| 2 | 0.72 | 0.68 | 0.70 | 0.63 |
| 2.5 | 0.68 | 0.6 | 0.65 | 0.54 |
| 3 | 0.65 | 0.44 | 0.60 | 0.42 |

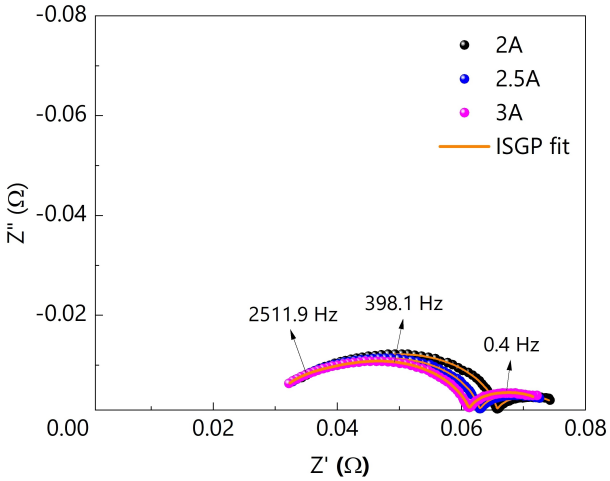


**Figure 2.** Nyquist plots of an $H_2$–$O_2$ AEMFC operated with 1 slpm gas flows at 80 °C with equal humidification (relative humidity of 88%) and back-pressurization (100 kPa) on both electrodes at different currents (2, 2.5 and 3 A).

Each peak represents a different relaxation process: series resistance that is comprised of ionic resistance in the membrane + electronic conductivity of the catalyst layer (P1), hydrogen oxidation reaction (HOR, P2), oxygen reduction reaction (ORR, P3), anode mass transfer (P4), and cathode mass transfer (P5).[29] A closer look at the DFRT (Figure 3b) reveals that the processes related to the cathode, P3 and P5, are more distributed, shown by the width of the peaks, which are two to three times wider than those related to the anode, P2 and P4, at each measured current.

Using the DFRT data, the effective resistance ($R_{eff}$) was calculated for each process by multiplying the peak area by the normalization factor (typically the real impedance at the lowest frequency). Figure 3c presents a comparison of the calculated values at 2, 2.5, and 3 A. Similar to the relaxation time trends in the DFRT plots, we see that the resistance values related to the cathode, P3 and P5 are two to three times higher than those related to the anode, P2 and P4, at each measured current. This strongly suggests that the cathode side (ORR process and cathode mass transfer) determines the overall performance of the AEMFC device.

Figure 3c further reveals that the highest resistance is due to the coupled effect of the membrane + electronic conductivity of the catalyst-layer, P1. The contributed $R_{eff}$ diminishes with drawn current, indicating that the $R_{eff}$ provided by P1 decreases with increasing current. The increased water in the AEM could be the cause for this phenomenon as the Grotthus (hopping) mechanism is enhanced given that higher water content could enhance ($OH^-$) ionic mobility. The electronic conductivity of the catalytic layers is assumed to remain constant at each current due to the fixed temperature. The 10,000 Hz high frequency limitation of the Scribner potentiostat, restricts our ability to decouple the equivalent series resistance into respective ionic resistance of the membrane and electronic conductivity of catalyst layer. It is unknown whether enhancing the high frequency limit would significantly improve the situation or not, as the peaks could be overlapped.

The HOR (P2) process improves with increased current. By this, we mean that the effective resistance decreases as a function of the drawn current revealing that HOR resistance is also a function of the current load.[52]

The ORR-contribution (P3) to $R_{eff}$ is slightly changed with current. This suggests that the humidification of oxygen before the cathode is sufficient, therefore drying or flooding of the cathode did not cause measurable changes in the resistance. The $R_{eff}$ of P3 is approximately 2.5-fold higher than that of P2, which lends credence to the fact that the ORR is the rate limiting reaction in the AEMFC. Unlike P2 & P3, the $R_{eff}$ calculated from peaks P4 and P5 increases with the drawn current. This indicates that water flooding at higher current densities impedes mass transfer at both anode and cathode sides. However, this flooding effect is noticeably higher on the cathode as the P5 peaks display greater $R_{eff}$ values than P4. This may be caused by the fact that the anode carbon content was higher than the cathode given that additional carbon was added to increase the pore volume and avoid flooding (see AEMFC fabrication under the experimental section below for more details). This resulting increased porosity as well as adjustment in hydrophobicity help to push more water away

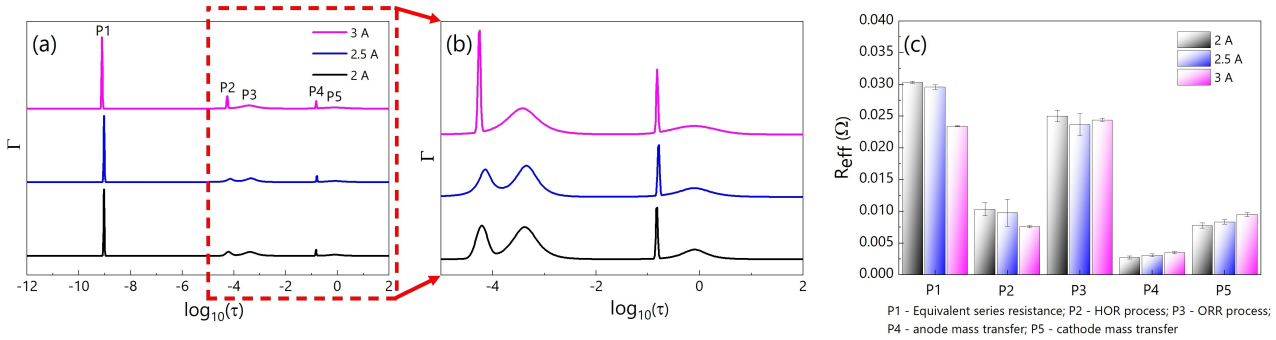


**Figure 3.** $H_2$–$O_2$ AEMFC operated with 1 slpm gas flows at 80 °C with equal humidification (relative humidity of 88%) and back-pressurization (100 kPa) on both electrodes. (a, b) Distribution function of relaxation time (DFRT) plots at different currents. (c) The corresponding calculated effective resistance ($R_{eff}$) values of each peak at the different currents, based on the area under each peak multiplied by the total resistance.

from the anode catalyst layer towards the membrane to the cathode catalyst layer.

An analysis of the EIS data with $H_2$—$O_2$ measured at a constant current load of 3 A without BP on both sides, 100 kPa on the anode only, 100 kPa on the cathode only and 100 kPa on both anode and cathode is presented by the Nyquist plots in Figure 4a. Both depressing and incomplete arcs can be seen within the measured frequency range. Here, the incomplete arc may be coming from the lower frequency limit that we set of 0.1 Hz. Going past 0.1 Hz may potentially complete the arc, but the change may simultaneously increase the frequency sweep data acquisition time-period and inadvertently introduce other experimental artifacts into the study and distort the data (see further details about ISGP and EIS data validity in the experimental section). Furthermore, adding BP of 100 kPa on both sides causes the incomplete arc to become a complete arc.

The diameters of the arcs change with back-pressurization, which suggests that the contributed resistances change. For ISGP analysis on the more reliable high frequency regions, the incomplete arcs were removed and the resultant DFRTs are shown in Figure 4b. This data provides evidence that the resistance contributed by the HOR process (P2), ORR process (P3), anode mass transfer (P4) and cathode mass transfer (P5) are highly dependent on the operating conditions. The removal of BP causes both P4 and P5 to be masked by an incomplete arc, which presents strong evidence that the absence of BP on both sides will affect the ORR reaction pathways.[26] The incomplete arc also masked P5 when 100 kPa of BP was applied independently ot he anode and cathode. On the other hand, when we apply BP to both sides, all five peaks are visible.

DFRT (Figure 4b) is used to calculate the $R_{eff}$ for each process (Figure 4c). In general, it seems that P4 and P5 are less reliable in this comparison as P5 is on the edge ot he measurement and is not detected in three ot he four cases at all. We observe that the relaxation times as well as the effective resistances attributed ot he ORR processes are higher than those associated with the anode (i.e. P3 > P2). Also, the AEMFC shows a low $R_{eff}$ for P1 without BP while in contrast the $R_{eff}$ value is not dramatically different when 100 kPa of BP is applied independently to either the anode or cathode. In contrast, the $R_{eff}$ value is not dramatically different when 100 kPa of BP was applied independently ot he anode and cathode. However, applying BP on both sides slightly reduces the ionic movement. We postulate that since the cell humidification was equal on both sides (relative humidity of 88%), the available water across the cell was not optimal. Operating the cell with higher humidification on the cathode, which is susceptible to drying and where the $OH^-$ ions are produced could possibly have improved this trend resulting in lower $R_{eff}$ and improved AEMFC performance. P2 with BP on both or either side showed slightly higher values than P2 without BP, which means the rate at which water is lost via convection is decreased when BP is applied,[53] resulting in increased water at the HOR site and higher $R_{eff}$.

As anticipated, the ORR contribution (P3) to $R_{eff}$ increases substantially when no BP is applied to the cathode. Applying BP to the cathode only or simultaneously to the anode and cathode results in enhanced ORR activity, which is directly related to the low $R_{eff}$ value.[54–55] The $R_{eff}$ is increased by removing BP at the cathode side (100 kPa on anode only). Therefore, BP on the cathode side is essential to accelerating the ORR kinetics. Nulling the BP at the cathode decreases mass diffusion on the anode side, which could be caused by anode flooding. By applying back-pressure on the cathode or to both sides, mass diffusion is improved on the anode.

With the change to $CO_2$-free air, one can observe a depressing arc within the measured frequency regions (Figure 5a). With an increase in drawn current, the high-frequency intersection changes slightly. By contrast, the low-frequency regions do not exhibit incomplete arcs in a $H_2$—$O_2$ atmosphere (as shown in Figure 2). In a reduced $O_2$ pressure, the incomplete arcs appear to be masking the mass transfer processes at the cathode. The low frequency data was cut (Figure 5b), and the remaining data fed into ISGP to understand the changes at mid and high frequencies. There is one out-of-range peak at high frequency (P1) and three peaks (P2, P3, P4) (Figure 5c) within the remaining range. Unfortunately, the P5 peaks of the prior $O_2$ experiment were not reflected here, as they may have been masked by the removed, incomplete arcs.[26]

Figure 5d shows the $R_{eff}$ values for each process. With currents up to 3 A, the $R_{eff}$ value of P1 does not change greatly. As compared to $H_2$—$O_2$, P1 has a $R_{eff}$ value close to the same. According to the results, P1 does not depend too much on the

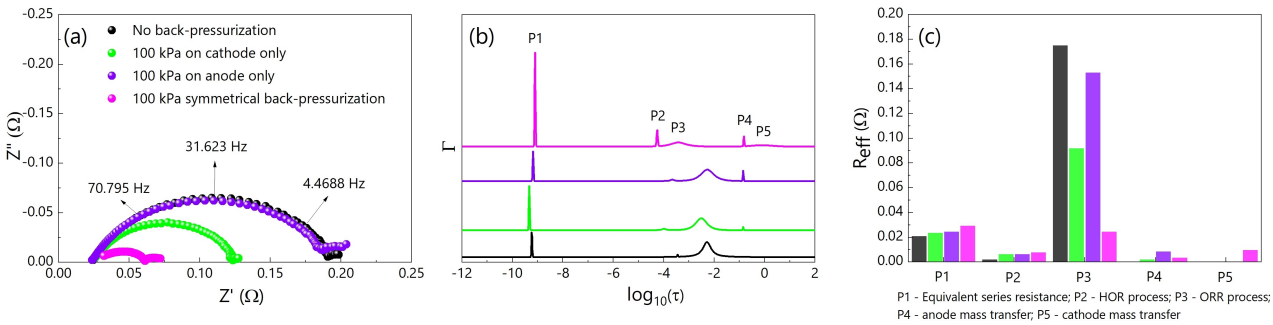


**Figure 4.** $H_2$—$O_2$ AEMFC operated with 1 slpm gas flows at 80 °C with equal humidification (relative humidity of 88%) and a constantly applied current of 3 A. Cell back-pressurization conditions varied between 100 kPa on both electrodes, 100 kPa on anode only, 100 kPa on cathode only and no BP. (a) Nyquist plots. (b) DFRT plots. (c) The calculated effective resistance values.

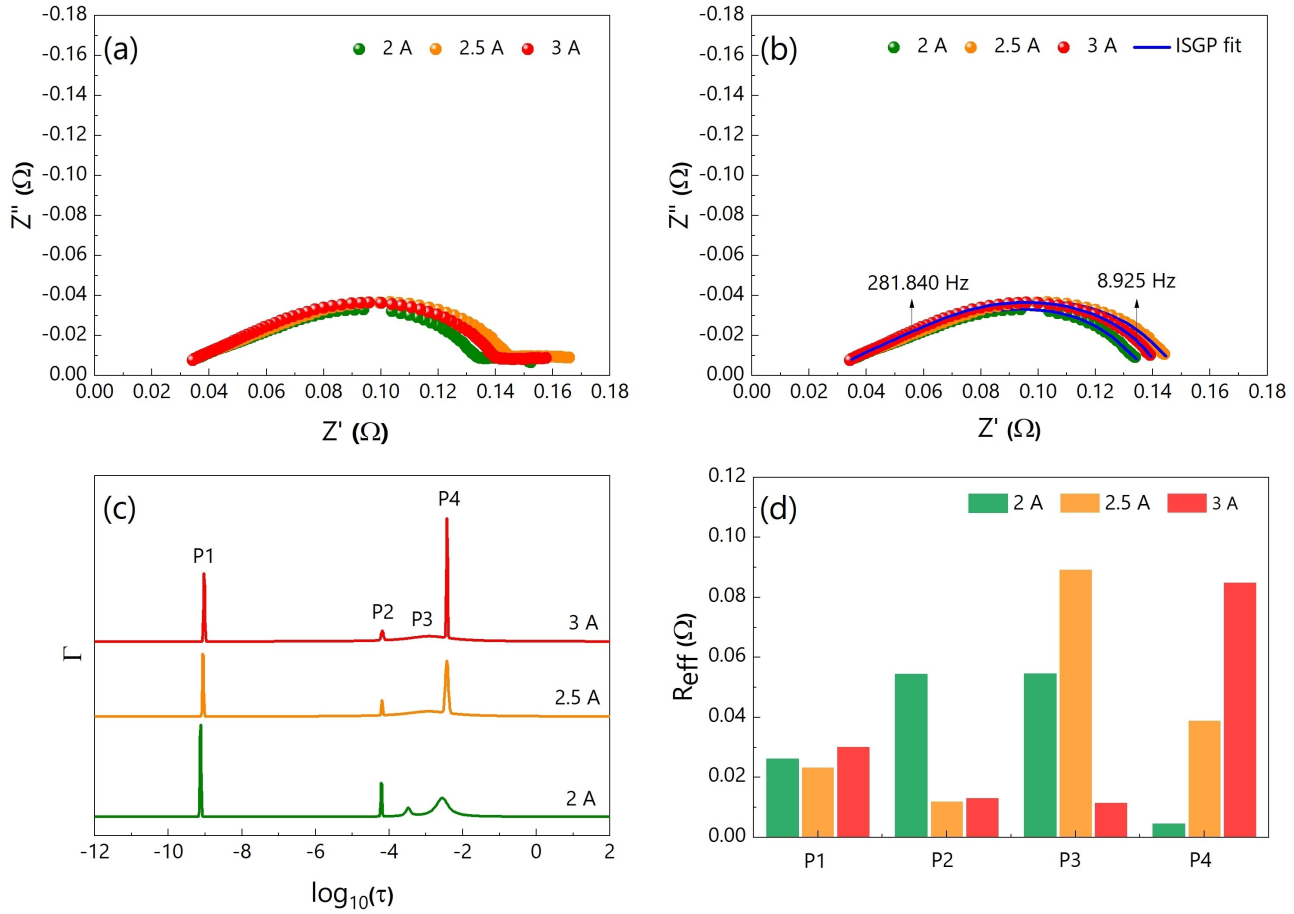


P1 - Equivalent series resistance; P2 - HOR process;
P3 - ORR process; P4 - anode mass transfer

**Figure 5.** Nyquist plots of AEMFC operated in $H_2$–$CO_2$-free air at different drawn currents (a) With and (b) Without the low frequency response. (c) DFRT plots at different drawn currents based on (b). (d) The calculated $R_{eff}$ values.

cathode oxidant. An increase in current up to 3 A decreases the $R_{eff}$ value of P2. Even though, the $R_{eff}$ value of P2 for $H_2$–$O_2$ is relatively low. A high $R_{eff}$ value is obtained for P3 in $H_2$–$CO_2$-free air at 2.5 A, possibly caused by a dry cathode (this is a speculation though). As the cathode hydration increases, the $R_{eff}$ value declines after 2.5 A. It is known that as current increases, water is generated at the anode in greater quantities, which in turn increases the amount of water transmitted through the membrane to the cathode side. Compared with $H_2$–$O_2$, with the exception of the 3 A current value, P3 (ORR related) exhibits a high $R_{eff}$ value in $H_2$–$CO_2$-free air. The high $R_{eff}$ may be caused by the reduced $O_2$ in the air. P4's $R_{eff}$ value increases as the drawn current increases. It could be caused by a large amount of water flooding at the anode, causing the mass transfer to be limited.

When $H_2$–$CO_2$-free air is used, the $R_{eff}$ values obtained are relatively higher than in the case of $H_2$–$O_2$. However, since these peaks were partially cut at the lower frequency side, the confidence of the measurements and capability of interpretation are limited.

## Conclusions

In summary, the ohmic region of a high performing operando AEMFC was analyzed using ISGP for the first time, specifically at constant discharge current loads of 2, 2.5 and 3 A. The ionic resistance in the membrane and catalyst layers, HOR, ORR, anode mass transfer, and cathode mass transfer phenomena were isolated at different relaxation times, and their contributing $R_{eff}$ were quantified and identified as P1, P2, P3, P4 and P5, respectively. For the first time shown in this work, we measured and quantified the individual $R_{eff}$ contributions of the simultaneous AEMFC processes. Building on that foundation, we showed the degree to which the $R_{eff}$ contributions vary as the operating conditions were changed and their impact on the AEMFC's performance. While operating with pure oxygen as the oxidant, the relaxation times and effective resistances related to the cathode (P3, P5) are two to three times higher than those related to the anode (P2, P4). This trend is similar when the cathode oxidant is switched to $CO_2$-free-air, however there are some instances in which the resistance is higher at the anode, particularly 2 A, indicating reduced cell hydration. This first-of-

its-kind study reveals that some of the losses are counter-intuitive and cannot be easily discerned without further insight.

We believe that this first work provides valuable information to the AEMFC community as it brings crucial understanding to all the catalytic and mass processes in this technology by helping to demystify what is occurring inside of an operating cell. Naturally, these phenomena may change when materials such as catalysts, membranes, and other components are adjusted, and they can be the focus of intriguing new research within the community. Further, given that there are other electrochemical reactions and systems that operate in closed environments, these findings could help spur further thoughts to a broader community of researchers including but not limited to those interested in platinum-group-metal (PGM) and PGM-free catalysis and devices using membrane electrode assemblies such as water electrolyzers, redox flow batteries, and other electrochemical systems where individual physical processes occur simultaneously and need to be sequestered for deeper understanding.

## Experimental Section

### Materials

Hydrogen, nitrogen and oxygen with 99.999% purity as well as $CO_2$-free air (21% oxygen) were purchased from Maxima, Israel. Carbon Black (Vulcan XC 72) was purchased from Cabot Corporation. PtRu/C catalyst (40% Pt and 20% Ru on carbon black, HiSPEC® 10000) and Pt/C catalyst (40% Pt on carbon black, HiSPEC® 4000) were purchased from Alfa Aesar. Radiation-grafted anion-exchange membranes (AEMs) containing covalently-bonded benzyltrimethylammonium (BTMA) head-groups (ion-exchange capacity of $2.49 \pm 0.12$ mmol g-1 and 55 μm hydrated thickness), fabricated from 25 μm thick low-density polyethylene (LDPE-BTMA) were used.[56–57] Anion-exchange ionomer (AEI), consisting of cross-linked polystyrene functionalized with trimethylamine was supplied by Fumatech BWT GmbH (Germany). Toray carbon paper TGP–H-060 with 5 wt% PTFE wet-proofing and PTFE gaskets were purchased from FuelCellStore.

### AEMFC Fabrication

AEMFCs were made via the gas diffusion electrode method using the materials mentioned herein and following the general procedures we previously reported elsewhere.[41–50] In brief, for the anode, 12 mg of PtRu/C catalyst was combined with 5 mg of AEI, and 6 mg of Vulcan XC 72 carbon and ground with a mortar and pestle. Carbon was added to increase the pore volume and avoid flooding. One-part of deionized water and nine-parts of isopropanol were added to the mixture and further ground to create a slurry (Figure S2). For the cathode, Pt/C catalyst was prepared in a similar manner to the anode, using 21 mg of Pt/C and combined with 5 mg of AEI (AEI:catalyst = 1:4). Gas diffusion layers were cut for the anode and cathode, to active area size of 2.25 $cm^2$. After ultrasonicating the inks at 180 W, 37 kHz for 1 h in a Elmasonic P 60 H ultrasonic bath filled with water and ice to keep the temperature below 10 °C, they were sprayed directly onto the gas diffusion layers (Figure S2) with an Iwata HP-TH professional airbrush and subsequently placed on a heater to dry for 5 seconds at 140 °C after each spray. After several repetitions of spraying and drying, the anode and cathode gas diffusion electrodes (GDEs) were periodically weighed in order to arrive at a final geometric precious metal loadings of 0.6 $mg_{PtRu}\,cm^{-2}$ and 0.55 $mg_{Pt}\,cm^{-2}$, respectively. The electrodes, along with a 6.25 $cm^2$ piece of the LDPE-BTMA AEM, were immersed in aqueous 1 M KOH solution for 1 h, with solution changes every 20 min, to convert to hydroxide form. The AEMFC was then assembled in-situ with PTFE gaskets each containing a 2.40 $cm^2$ cutout in the center to expose enough of the membrane on either side for the electrodes to make contact with. The membrane electrode assembly was placed between two 5 $cm^2$ single-serpentine graphite flow field plates (Figure S2) and the fuel cell test hardware closed using 4.5 N-m of torque to obtain a pinch of 25%.

### AEMFC Testing

The AEMFCs were tested in an 850E Scribner Associates Fuel Cell test station. The cell temperature was first heated up while flowing 99.999% $N_2$ at 0.25 slpm and allowed to stabilize at a cell, anode, and cathode temperatures of 80 °C, then fed with pure humidified 99.999% $H_2$ and 99.999% $O_2$ reactant gases at flow rates of 1 slpm without back-pressurization (see Figure S3 for operational schematic). The cell voltage was decreased to 0.5 V at which point the anode and cathode relative humidities were optimized to 88%, where a maximum and stable current density of ~1.25 $A\,cm^{-2}$ was obtained. Then, backpressures were increased to 100 kPa on both electrodes, which increased the maximum current density to 2.5 $A\,cm^{-2}$. This was followed by a polarization curve from 1.1 to 0.1 V, recorded at a scan rate of 5 $mV\,s^{-1}$ to capture beginning-of-life performance and mitigate against any degradation-related power losses. Additional polarization curves were also captured after any adjustments to the operating conditions were made to the cell such as backpressure adjustments (no back-pressurization, 100 kPa on the anode only and 100 kPa on the cathode only) as well as when the cathode oxidant switched to $CO_2$-free air (21% $O_2$).

### Acquisition of Electrochemical Impedance Spectroscopy Data

Immediately after polarizing the cell under $H_2$—$O_2$, the current was set to 2 A (0.89 $A\,cm^{-2}$) and the frequencies were swept over the range of 0.1 to 10,000 Hz with 20 points per decade with an alternating current perturbation of 5% of the operating direct current. The sweeps were repeated ten times and collated to obtain an ideal picture of the Nyquist plot given that slight deviations can occur over time. Then the current was increased to and held at 2.5 A (1.11 $A\,cm^{-2}$) then 3 A (1.33 $A\,cm^{-2}$) to repeat the frequency sweeps. Additional frequency sweeps were also conducted while the current was held at 3 A on the cell without backpressure, 100 kPa on the anode only and 100 kPa on the cathode only. After acquiring the EIS data with $O_2$ flowing on the cathode, the cathode oxidant was switched to $CO_2$-free air and back-pressures of 100 kPa was applied to both electrodes while all other operating conditions were held constant. Seven polarization curves were performed to ensure no substantial losses in performance. After verifying stability, the current was set to 2, 2.5, and 3 A, respectively, and corresponding EIS data acquired in the manner described above. Back-pressurization (BP) was further adjusted at the 3 A current load to investigate the effects of no BP as well as the independently pressurized anode and cathode. Following the acquisition of the EIS data, it was transferred to ISGP for further analysis (Figure S4).

### Impedance Spectroscopy Genetic Programming (ISGP)

ISGP is MATLAB based genetic algorithm, which was developed in the Tsur research group at the Technion – Israel Institute of

Technology.[58] The impedance can be written as a Fredholm equation of the second kind (Eq. 1):[58]

$$Z(\log(\omega)) = R_{\infty} + R_{pol}\int_{-\infty}^{\infty}\frac{\Gamma(\log(\tau))}{i+i\omega\tau}d(\log(\tau)) \quad (1)$$

Where, Z(ω), $R_{\infty}$, $R_{pol}$, Γ, τ, and ω represent the impedance, equivalent series resistance, total polarization resistance, the distribution function of relaxation times (DFRT), relaxation time, and angular frequency, respectively. Data validity is assessed by Kramers-Kronig (K–K) transformation. Because experimental artifacts can sometimes distort the EIS data, the K–K transformation is relied upon to provide useful insight into the validity of the data. In the event that the data passes K–K transformation, we set the number of assumed peaks and some other user options, such as the type of peak used by the program, a completion criterion, etc., and run the program. The inverse problem presented in equation 1 can be solved by applying Tikhonov regularization or other inverse approaches, yielding a point-by-point function. In contrast, ISGP uses a direct approach and finds an analytical function using an evolutionary algorithm.

An ISGP begins with a set of linear combinations of known mathematical functions called DFRT models. DFRT models are doubled in number, and their compatibility with measured data and other factors are assessed. New sets of models are generated from certain 'mutations' of the highest graded models. Afterward, each new DFRT model is graded, and the highest graded models are chosen to continue on. A model selected by evolutionary pressure will be the most compatible with the measured data, but also the one with the least number of peaks and the fewest number of free parameters per peak to avoid over-fitting.

The output of an ISGP analysis is shown in Figure S4, with the normalized Nyquist plot shown in Figure S4a. Herein, the spherical shape and solid line within the measured region range corresponds to experimental and synthetic data, respectively. The experimental data points are well fitted with the synthetic data. In Figure S4b, the DFRT plot shows an out-of-range peak at low relaxation time or high frequency. Within the measured frequency, four peaks are clearly seen. The area under the peaks is different, which indicates that the resistance contributed by each process is different. In Figure S4c, the smaller residual value confirms good fitting.

The discrepancy-complexity plots are shown in Figure S4d. The ISGP program chooses the first population randomly, which leads to generate the models with high discrepancy and different complexities. In the next step, the program reduces the unnecessary complexity and produces simple and better-fitting models. Furthermore, the program suppresses the discrepancy between experimental data and synthetic data. The red diamond mark indicates the lower discrepancy value and best-fitted model (Figure S4f). The compatibility value is closer to 0.9 (Figure S4e), which confirms a good fit between the experimental and predicted model.

## Author Contributions

J.C.D. and K.V.S. contributed equally with obtaining, analyzing, and compiling the data as well as all stages of writing. A.L.G.B. and E.I.S. supplied the membranes and helped with writing. Y.T. acquired funding, participated in the analysis, and was involved in all stages of writing. D.R.D. acquired funding, initiated the research, set the goals, participated in the analysis, and was involved in all stages of writing.

## Acknowledgements

This work was partially funded by the Nancy & Stephen Grand Technion Energy Program (GTEP); by the Ministry of National Infrastructure, Energy and Water Resources of Israel through grant No. 3-16686 (219-11-135) and through grant No. 3-17591 (220-11-040); the Israel Science Foundation (grants number 2002/22 and 169/22); and the European Union's Horizon 2021 research and innovation program, under grant agreement 101071111. A.L.G.B. acknowledges FAPESP grant No. 2019/26955-3. E.I.S. acknowledges CINE/SHELL (ANP)/FAPESP grant No. 2017/11937-4 and CNPq for financial support. J.C.D. personally wishes to thank Dr. Irwin and Mrs. Joan Jacobs for their generous financial support in the form of the Jacobs Excellence Scholarship. J.C.D. also personally wishes to thank The Israeli Smart Transportation Research Center for their generous financial support in the form of the ISTRC Scholarship. We thank the Israel National Research Center for Electrochemical Propulsion (INREP) funded by the Planning & Budgeting Committee/Israel Council for Higher Education, and the Israel Fuel Cells Center (IFCC) for their continued support.

## Conflict of Interests

The authors declare no conflict of interest.

## Data Availability Statement

The data that support the findings of this study are available from the corresponding author upon reasonable request.

**Keywords:** Anion exchange · Fuel cells · Heterogeneous catalysis · Impedance spectroscopy · Membranes

[1] C. Bailey, A. Bain, J. Birk, M. Hainsselin, M. Kamal, H. Linden, A. Lloyd, F. Lynch, J. Mackenzie, D. Nahmias, *National Renewable Energy Laboratory (NREL): Washington, DC, USA* **1995**.
[2] P. P. Edwards, V. L. Kuznetsov, W. I. F. David, N. P. Brandon, *Energy Policy* **2008**, *36*, 4356–4362.
[3] I. Staffell, D. Scamman, A. V. Abad, P. Balcombe, P. E. Dodds, P. Ekins, N. Shah, K. R. Ward, *Energy Environ. Sci.* **2019**, *12*, 463–491.
[4] J. R. Varcoe, P. Atanassov, D. R. Dekel, A. M. Herring, M. A. Hickner, P. A. Kohl, A. R. Kucernak, W. E. Mustain, K. Nijmeijer, K. Scott, T. Xu, L. Zhuang, *Energy Environ. Sci.* **2014**, *7*, 3135–3191.
[5] S. Gottesfeld, D. R. Dekel, M. Page, C. Bae, Y. Yan, P. Zelenay, Y. S. Kim, *J. Power Sources* **2018**, *375*, 170–184.
[6] D. R. Dekel, *J. Power Sources* **2018**, *375*, 158–169.
[7] J. Biemolt, J. C. Douglin, R. K. Singh, E. S. Davydova, N. Yan, G. Rothenberg, D. R. Dekel, *Energy Technol.* **2021**, *9*.
[8] A. Sarapuu, E. Kibena-Põldsepp, M. Borghei, K. Tammeveski, *J. Mater. Chem. A* **2018**, *6*, 776–804.
[9] M. M. Hossen, M. S. Hasan, M. R. I. Sardar, J. B. Haider, Mottakin, K. Tammeveski, P. Atanassov, *Appl. Catal. B* **2023**, *325*, 121733.
[10] C. G. Arges, V. K. Ramani, P. N. Pintauro, *Electrochem. Soc. Interface* **2010**, *19*, 31–35.

[11] H.-S. Shiau, A. Z. Weber, *ECS Meeting Abstracts* **2016**, *MA2016-02*, 2395–2395.
[12] A. Kabza, *Fuel cell formulary* **2015**.
[13] P. K. Das, D. Thumbarathy, *in Convective Heat Transfer in Porous Media*, CRC Press, **2019**, pp. 341–360.
[14] H.-S. Shiau, I. V. Zenyuk, A. Z. Weber, *J. Electrochem. Soc.* **2017**, *164*, E3583-E3591.
[15] K. Yassin, I. G. Rasin, S. Brandon, D. R. Dekel, *J. Membr. Sci.* **2020**, *608*, 118206.
[16] B. Eriksson, H. Grimler, A. Carlson, H. Ekström, R. Wreland Lindström, G. Lindbergh, C. Lagergren, *Int. J. Hydrogen Energy* **2019**, *44*, 4930–4939.
[17] W. E. Mustain, M. Chatenet, M. Page, Y. S. Kim, *Energy Environ. Sci.* **2020**, *13*, 2805–2838.
[18] J. Zhou, J. Guo, D. Chu, R. Chen, *J. Power Sources* **2012**, *219*, 272–279.
[19] Y. Zhao, J. Pan, H. Yu, D. Yang, J. Li, L. Zhuang, Z. Shao, B. Yi, *Int. J. Hydrogen Energy* **2013**, *38*, 1983–1987.
[20] J. N. Schwämmlein, N. L. T. Pham, T. Mittermeier, M. Egawa, L. Bonorand, H. A. Gasteiger, *J. Electrochem. Soc.* **2020**, *167*, 084513.
[21] J. Leppin, C. Clark, J. Behnken, C. Harms, A. Dyck, *ECS Trans.* **2018**, *86*, 629–642.
[22] J. R. Varcoe, R. C. T. Slade, G. L. Wright, Y. Chen, *J. Phys. Chem. B* **2006**, *110*, 21041–21049.
[23] D. Yang, H. Yu, G. Li, Y. Zhao, Y. Liu, C. Zhang, W. Song, Z. Shao, *J. Power Sources* **2014**, *267*, 39–47.
[24] X. Xie, J. Zhou, S. Wu, J. W. Park, K. Jiao, *Int. J. Chem. Res.* **2019**, *43*, 8522–8535.
[25] X. Gao, H. Yu, J. Jia, J. Hao, F. Xie, J. Chi, B. Qin, L. Fu, W. Song, Z. Shao, *RSC Adv.* **2017**, *7*, 19153–19161.
[26] T. Reshetenko, M. Odgaard, D. Schlueter, A. Serov, *J. Power Sources* **2018**, *375*, 185–190.
[27] M. Hwang, R. Sun, C. Willis, Y. A. Elabd, *Fuel Cells* **2020**, *20*, 624–633.
[28] A. Carlson, P. Shapturenka, B. Eriksson, G. Lindbergh, C. Lagergren, R. Wreland Lindström, *Electrochim. Acta* **2018**, *277*, 151–160.
[29] M. Hu, Q. Li, H. Peng, H. Ma, L. Xiao, G. Wang, J. Lu, L. Zhuang, *J. Power Sources* **2020**, *472*, 228471.
[30] B. A. Boukamp, *Electrochim. Acta* **2015**, *154*, 35–46.
[31] M. Saccoccio, T. H. Wan, C. Chen, F. Ciucci, *Electrochim. Acta* **2014**, *147*, 470–482.
[32] A. L. Gavrilyuk, D. A. Osinkin, D. I. Bronin, *Russ. J. Electrochem.* **2017**, *53*, 575–588.
[33] T. Horlin, *Solid State Ionics* **1993**, *67*, 85–96.
[34] G. Avioz Cohen, D. Gelman, Y. Tsur, *J. Phys. Chem. C* **2021**, *125*, 11867–11874.
[35] N. Bar, P. Basak, Y. Tsur, *Phys. Chem. Chem. Phys.* **2017**, *19*, 14615–14624.
[36] A. K. Baral, Y. Tsur, *Solid State Ionics* **2017**, *304*, 145–149.
[37] V. S. Kalimuthu, R. Attias, Y. Tsur, *Electrochem. Commun.* **2020**, *110*, 106641.
[38] A. Kumar Baral, K. Vijaya Sankar, A. Matatyaho, G. Kushnir, Y. Tsur, *ChemSusChem.* **2020**, *13*, 5671–5682.
[39] B. Malik, K. Vijaya Sankar, S. K. T. Aziz, S. Majumder, Y. Tsur, G. D. Nessim, *J. Phys. Chem. C.* **2021**, *125*, 23126–23132.
[40] A. Oz, D. Gelman, E. Goren, N. Shomrat, S. Baltianski, Y. Tsur, *J. Power Sources* **2017**, *355*, 74–82.
[41] K. Aggarwal, S. Bsoul, J. C. Douglin, S. Li, D. R. Dekel, C. E. Diesendruck, *Chem. - Eur. J.* **2022**, *28*.
[42] A. L. G. Biancolli, S. Bsoul-Haj, J. C. Douglin, A. S. Barbosa, R. R. de Sousa, O. Rodrigues, A. J. C. Lanfredi, D. R. Dekel, E. I. Santiago, *J. Membr. Sci.* **2022**, *641*, 119879.
[43] J. C. Douglin, R. K. Singh, E. R. Hamo, M. B. Hassine, P. J. Ferreira, B. A. Rosen, H. A. Miller, G. Rothenberg, D. R. Dekel, *J. Solid State Electrochem.* **2022**, *26*, 2049–2057.
[44] J. C. Douglin, J. R. Varcoe, D. R. Dekel, *Journal of Power Sources Advances* **2020**, *5*, 100023.
[45] E. R. Hamo, R. K. Singh, J. C. Douglin, S. Chen, M. B. Hassine, E. Carbo-Argibay, S. Lu, H. Wang, P. J. Ferreira, B. A. Rosen, D. R. Dekel, *ACS Catal.* **2021**, *11*, 932–947.
[46] T. Huang, G. He, J. Xue, O. Otoo, X. He, H. Jiang, J. Zhang, Y. Yin, Z. Jiang, J. C. Douglin, D. R. Dekel, M. D. Guiver, *J. Membr. Sci.* **2020**, *597*, 117769.
[47] M. Kumari, J. C. Douglin, D. R. Dekel, *J. Membr. Sci.* **2021**, *626*, 119167.
[48] S. Wierzbicki, J. C. Douglin, A. Kostuch, D. R. Dekel, K. Kruczała, *J. Phys. Chem. Lett.* **2020**, *11*, 7630–7636.
[49] S. Wierzbicki, J. C. Douglin, R. K. Singh, D. R. Dekel, K. Kruczała, *ACS Catal.* **2023**, 2744–2750.
[50] K. Yassin, J. C. Douglin, I. G. Rasin, P. G. Santori, B. Eriksson, N. Bibent, F. Jaouen, S. Brandon, D. R. Dekel, *Energy Convers. Manage.* **2022**, *270*, 116203.
[51] M. J. Kim, O.-H. Kim, S. Kim, Y.-W. Choi, Y.-H. Cho, Y.-E. Sung, *J. Ind. Eng. Chem.* **2018**, *61*, 437–444.
[52] Y. Zheng, T. J. Omasta, X. Peng, L. Wang, J. R. Varcoe, B. S. Pivovar, W. E. Mustain, *Energy Environ. Sci.* **2019**, *12*, 2806–2819.
[53] T. J. Omasta, X. Peng, H. A. Miller, F. Vizza, L. Wang, J. R. Varcoe, D. R. Dekel, W. E. Mustain, *J. Electrochem. Soc.* **2018**, *165*, J3039-J3044.
[54] J. Lilloja, E. Kibena-Põldsepp, A. Sarapuu, J. C. Douglin, M. Käärik, J. Kozlova, P. Paiste, A. Kikas, J. Aruväli, J. Leis, V. Sammelselg, D. R. Dekel, K. Tammeveski, *ACS Catal.* **2021**, *11*, 1920–1931.
[55] N. Ul Hassan, M. Mandal, G. Huang, H. A. Firouzjaie, P. A. Kohl, W. E. Mustain, *Adv. Energy Mater.* **2020**, *10*.
[56] A. L. G. Biancolli, A. S. Barbosa, Y. Kodama, R. R. de Sousa, A. J. C. Lanfredi, F. C. Fonseca, J. F. Q. Rey, E. I. Santiago, *J. Power Sources* **2021**, *512*, 230484.
[57] A. S. Barbosa, A. L. G. Biancolli, A. J. C. Lanfredi, O. Rodrigues, F. C. Fonseca, E. I. Santiago, *J. Membr. Sci.* **2022**, *659*, 120804.
[58] S. Hershkovitz, S. Tomer, S. Baltianski, Y. Tsur, *ECS Trans.* **2011**, *33*, 67–73.

Manuscript received: July 27, 2023
Revised manuscript received: July 30, 2023
Accepted manuscript online: July 31, 2023
Version of record online: September 28, 2023